

Phase coherent transport in bilayer and trilayer MoS₂

Leiqiang Chu,^{1,2*} Indra Yudhistira,^{1,3*} Hennrik Schmidt,^{1,3} Tsz Chun Wu,⁵ Shaffique Adam,^{1,3,6,†} and Goki Eda^{1,3,4,‡}

¹*Department of Physics, National University of Singapore, 3 Science Drive 3, Singapore 117543*

²*Department of Physics, Shaoxing University, Shaoxing, China, 312000*

³*Centre for Advanced 2D Materials and Graphene Research Centre, National University of Singapore, 6 Science Drive 2, Singapore 117546*

⁴*Department of Chemistry, National University of Singapore, 2 Science Drive 3, Singapore 117551*

⁵*Department of Physics and Astronomy, Rice University, Houston, Texas 77005, USA*

⁶*Yale-NUS College, 6 College Ave West, Singapore 138614*

Abstract:

Bilayer MoS₂ is a centrosymmetric semiconductor with degenerate spin states in the six valleys at the corners of the Brillouin zone. It has been proposed that breaking of this inversion symmetry by an out-of-plane electric field breaks this degeneracy, allowing for spin and valley lifetimes to be manipulated electrically in bilayer MoS₂ with an electric field. In this work, we report phase-coherent transport properties of double-gated mono-, bi-, and tri-layer MoS₂. We observe a similar crossover from weak localization to weak anti-localization, from which we extract the spin relaxation time as a function of both electric field and temperature. We find that the spin relaxation time is inversely proportional to momentum relaxation time, indicating that D'yakonov-Perel mechanism is dominant in all devices despite its centrosymmetry. Further, we found no evidence of electric-field induced changes in spin-orbit coupling strength. This suggests that the interlayer coupling is sufficiently weak and that electron-doped dichalcogenide multilayers behave electrically as decoupled monolayers.

* L. C. and I. Y. contributed equally to this work.
Email: g.eda@nus.edu.sg

I. INTRODUCTION

Group 6 layered transition metal dichalcogenides (TMDs) emerged as promising candidates for spintronics and valleytronics due to their unique crystal structures and strong spin-orbit interaction [1,2]. Since they are centrosymmetric for even number of layers and non-centrosymmetric for odd number of layers, they provide a unique platform for systematically studying spin and valley physics. Understanding the interplay between these quantum degrees of freedom is key to developing novel device concepts [3,4]. The spin-valley coupling effect has been widely investigated by optically circularly polarized excitation in monolayers, which makes the valley polarization possible [5,6]. In bilayer TMDs, the inversion symmetry can be broken by an external out-of-plane electric field, allowing electrical control of their physical properties [7,8]. Applying an out-of-plane electric field in bilayer TMDs breaks valley degeneracy and recovers spin-valley locking that is unique in odd-layer materials. Correspondingly, the spin and valley lifetime dynamics is predicted to change with application of electric and magnetic field [9]. Using electric field to restore the spin-valley coupling in optical-electrical measurement has been demonstrated in device concepts [10,11]. Meanwhile, electric-field tunability of quantum interference effect in multi-layer and bulk TMDs has been realized experimentally through quantum interference effect in magneto-transport study with ionic liquid gating in the metallic state [12-14].

The effective electrical control of spin-orbit coupling strength is of great interest to the realization of spin- and valleytronic devices. However, field-induced effects in multi-layer TMDs are multifold and complex, and their impact on the experimentally measurable quantities remains elusive. Though quantum transport studies in multilayer by ionic gating manifest valley-contrasting properties, charge carriers also occupy the other valleys such as Λ point between the Γ and K points, which could inhibit the spin relaxation dynamics. However, for few-layer system such as in 1-3L MoS₂, the band minimum could lie in the K-point [15]. The reduced effect from other valleys could uncover the spin relaxation dynamics with symmetry argument as a function of thickness. Here, we present a comprehensive theoretical and experimental studies on the effect of out-of-plane electric field on spin-orbit interaction strength in electron-doped mono-, bi-, and trilayer MoS₂ through phase-coherent quantum transport. Our findings show that a significantly large electric field

is needed to achieve sizeable changes in spin-orbit coupling strength due to weak interlayer coupling of the conduction band electrons.

II. RESULTS AND DISCUSSION

We start with our theoretical modelling of the electric field-induced effect. The tunability of Zeeman-type spin splitting in bilayer TMDs with broken inversion symmetry are sensitive to two factors: conduction (valence) band interlayer hopping strength for electrons (holes) [9] and Bychkov-Rashba (BR) spin-orbit coupling strength [16]. BR spin-orbit coupling causes the vertically applied electric field in inversion asymmetric 2D electron gas to generate an in-plane effective magnetic field B_{BR}^{eff} , which could be superimposed to the Zeeman field, facilitating the intravalley spin flip. In Fig. 1(a), we show theoretical calculation of the dependence of the magnitude of intrinsic spin splitting $|\lambda_{int}|$ on interlayer electric field E_m for different conduction band interlayer hopping strength t_{\perp}^c within a minimal band model of bilayer TMDs in the vicinity of the K points [9,17]. The insets show the configuration of the electric field perpendicular to the atomic plane (up) and electronic structure in the absence and presence of external electric field E_m at the K point (down). With electric field applying, the inversion symmetry breaking lifts up spin degeneracy at Brillouin K points. We can see that λ_{int} vanishes for $|E_m|=0$, suggesting no spin splitting in pristine bilayer MoS₂, in agreement with the symmetry argument. We found that in the limit of vanishing t_{\perp}^c , the spin splitting $|\lambda_{int}|$ saturates rapidly as soon as E_m becomes non-zero and $|\lambda_{int}|$ increases slower with increasing $|E_m|$ as t_{\perp}^c gets larger. In Fig. 1(b), we show theoretical calculation of the dependence of spin splitting $|\lambda_{int}|$ on interlayer electric field E_m for different Bychkov-Rashba spin-orbit coupling strength λ_{BR} , within the same model. We found that for non-zero λ_{BR} , spin splitting λ_{int} increases as $|E_m|$ gets larger. In this case, increasing $|E_m|$ can be understood as increasing in-plane effective magnetic field, thereby increasing total effective magnetic field. However, for this effect to be noticeable, the strength of λ_{BR} has to be at least an order of magnitude larger than the value reported in Ref. [16]. Hence, the tunability of spin splitting requires either strong conduction (valence) band

interlayer hopping strength for electrons (holes) or strong Bychkov-Rashba spin-orbit coupling. In both Fig. 1(a) and (b), we have set the carrier type to be electron, which is in accordance with our experiment. In our theoretical model, the range of E_m has been estimated using self-consistent model of screening [17,18].

We now discuss the quantum coherent transport experimental results. The inset of Fig. 2(a) shows a schematic illustration of our double gate device with an ion-gel top gate and solid Si back gate. Details on the device preparation have been discussed in our previous work [19]. All of charge- and magneto-transport measurements were conducted in a Helium-4 cryostat. Figure 2(a) shows the back-gate charge transfer curves for 1L, 2L, and 3L MoS₂ devices at three different top gate voltages (0 V, 1 V, 1.7 V), respectively. The transfer curves are individually shifted horizontally to match their threshold voltage for each curve. V_{bg}^{eff} is the effective back-gate voltage corresponding to the total density in the 2D systems[19]. The charge densities are calculated with a capacitor model according to $n = C_{ox} (V_{bg}^{eff} - V_0)/e$, where C_{ox} is the gate capacitance, and $V_0 = -220.3$ V is determined by extrapolation of phase coherence length L_ϕ to 0 nm [17]. This nearly linear dependence of L_ϕ on V_{bg}^{eff} works well when the channel conductivity is larger than the conductance quantum. The charge carrier concentration then can be estimated to vary between 0.9×10^{13} and $4.7 \times 10^{13}/\text{cm}^2$ for the entire voltage range. The dashed lines in Figure 2(a) are fits to the conductivity according to $\sigma = \alpha (V_{bg}^{eff} - V_0)^\beta$ where α and β are fitting parameters. β is slightly larger than unity, indicating the superlinear dependence of σ on V_{bg}^{eff} . For the data present in Fig 2(a), the electronic transport is diffusive, similar to our previous work on monolayer MoS₂ [20]. The mean free path l and momentum relaxation time τ_p are therefore seen by $l = v_F \tau_p$ and $\tau_p = m^* \mu / e$ for mobility μ , carrier density n , electron charge e and effective mass m^* . The contact resistance is expected to play a minor role in this high doping regime due to the negligibly small depletion region [21].

For the double gate configuration, the average vertical electrical displacement field induced by combination of the two gates can be estimated with simple formula $D_m = (\kappa_{ox} V_b / d_b - \kappa_{ig} V_t / d_t) / 2$ [22,23], with $d_t \approx 1$ nm and $d_b = 300$ nm the thickness

of the top and bottom dielectric, $\kappa_{ox} \approx 3.9$ and $\kappa_{ig} \approx 7$ [24] the dielectric constant for SiO₂ and ion gel, and V_t and V_b the top and bottom gate voltages, respectively [23]. Here we assume the charge neutral point is at zero gate voltage. The direction of the external electric field is defined in inset to Fig. 1(a). Note that this formula doesn't take interlayer charge density imbalance into account. As seen in the figure, the electric displacement field falls in the range of about 4 V/nm, an overestimation of about an order of magnitude compared to the theoretical model employing self-consistent screening. This big discrepancy shows the importance of using the self-consistent screening theory to obtain the correct value of interlayer electric field in 2D parabolic system. This perpendicular electric field breaks the inversion symmetry of the bilayer system.

A perpendicular magnetic field breaks time reversal symmetry and leads to decoherence of the “closed-loop” current paths thereby suppressing WL, and generating a positive magnetoconductance $\Delta\sigma$. Figure 3 shows $\Delta\sigma$ as a function of both temperatures and gate voltages for 1~3L devices. The as-measured magnetoconductance curves were symmetrized to eliminate contributions from the sample geometry and Hall effect. Our analysis reveals that the magnetoresistance (MR) at high magnetic field is subjected to quadratic field dependent magnetoresistance containing both classical and quantum contributions. The pure quantum interference effect is extracted by subtracting the classical background [17]. As seen from the right panels of Figure 3, all devices exhibit a qualitatively similar trend characterized by positive $\Delta\sigma$ at low fields and a downward-turn at higher fields. This represents a crossover from WL to WAL with increasing fields, similar to our previous observation in monolayer MoS₂. The left side of each panel shows the theoretical fits, according to the Hikami-Larkin-Nagaoka (HLN) formula [25],

$$\Delta\sigma = g_l \frac{e^2}{\pi h} \left[F\left(\frac{B}{B_\phi}\right) - 3F\left(\frac{B}{B_\phi + 2B_{SO}}\right) \right], \quad (1)$$

where g_l represents the layer degeneracy, $F(Z)$ is defined by $F(z) = \ln(z) + \psi(1/2 + 1/z)$ with ψ the digamma function, $B_\phi = \hbar/4eL_\phi^2$ and $B_{SO} = \hbar/4eL_{SO}^2$ are fitting parameters associated with the effective magnetic field for the phase coherence length and crossover length, respectively. We found that the

formula with $g_l = 1, 2, 3$ for monolayer, bilayer, and trilayer, respectively yields much better fittings of the experimental results.

We apply the same analysis from our previous work [20] in order to extract the spin lifetime from the WL-WAL crossover. Briefly, because of the large separation of length scales, the crossover can be attributed to symmetry breaking due to spin-flip scattering. The spin-conserved intervalley scattering is expected to break the valley-rotational symmetry due to high defect density in MoS₂, mainly in the form of chalcogen vacancies. By conducting a two-parameter fit to the temperature- and magnetic field-dependent magneto-conductance curves according to Eq. (1), we obtain the spin lifetime τ_{so} from the relation $B_{so} = \hbar/4eD\tau_{so}$, where D is the classical diffusion constant.

Figure 4 shows the ratio of spin relaxation time τ_{so} divided by number of layers g_l as a function of inverse momentum relaxation time τ_p^{-1} , with inset showing a zoom in of the low spin relaxation time region. It can be seen that τ_{so} scales linearly with τ_p^{-1} in the entirely range, indicating that the dominant spin relaxation mechanism in all the samples is D'yakonov-Perel (DP) type where spin precesses between scattering events from disorder impurities or non-magnetic defects. It is worth noting that bilayer MoS₂ exhibits the same DP behavior despite being inversion symmetric. From the slope of the fitted dashed line, the spin-orbit coupling strength λ_{int} can be determined using the relationship $\tau_{so} = (2\hbar^2/\lambda_{int}^2)\tau_p^{-1}$. The strength of spin-orbit interaction λ_{int} of monolayer, bilayer and trilayer are found to be 7.2 meV, 6 meV, and 4.1 meV, respectively. These values represent the size of the conduction band splitting at the K point due to spin-orbit coupling. Similar trends for 1~3L devices and good agreement with Eq. (1) indicate that few-layer MoS₂ effectively behaves as g_l decoupled monolayers.

Comparing with the theoretically predicted behavior (Figure 1), the absence of electrically tunable spin-orbit splitting energy in all 1~3L devices implies the following: First, the Bychkov-Rashba spin-orbit coupling strength λ_{BR} is too weak to give rise to measurable changes in the spin-orbit interaction within the experimentally accessible electric field ranges. Second, a small perpendicular electric field is sufficient to break the inversion symmetry of bilayer MoS₂, lifting the spin

degeneracy at the Brillouin Zone corner. Third, the interlayer hopping for electrons at the K points is negligible as expected from the symmetry argument [9]. Thus, once the inversion symmetry of bilayer is broken, it soon becomes two decoupled monolayers and tuning the spin-orbit interaction strength becomes difficult, which in turn explains the good fitting when including g_l in Eq. (1).

III. CONCLUSION

In this work, we have presented the coherent quantum electron transport properties of double-gated mono-, bi-, and trilayer MoS₂. We observed qualitatively similar crossover from WL to WAL in all the devices. The crossover can be explained by HLN formula with the spin-orbit scattering as symmetry breaking crossover parameter. Despite having different symmetries, all the samples exhibited spin relaxation due to DP mechanism. This implies that the breaking of inversion symmetry due to out-of-plane electric fields is not sufficient to tune the spin-relaxation rate. We conclude that this lack of electric-field induced changes in spin-orbit interaction strength implies weak Bychkov-Rashba spin-orbit coupling strength λ_{BR} in TMD multilayers and a vanishing of interlayer coupling in the conduction band, which renders the bilayer system to behave like two decoupled monolayers. In contrast to conduction-band electrons, the interlayer hopping for valence band holes is finite (86 meV, Ref. [9]), and we therefore predict that a similar experiment performed instead on valence band holes would show a strong electric field tunability of the spin lifetimes.

Notes added:

After completion of this manuscript, we became aware of a similar work [26] that studied the phase-coherent transport properties of single-gated bilayer MoS₂ encapsulated in hexagonal boron nitride. The authors find τ_{so} is almost constant with carrier density. In contrast to our results in dual-gated ion-gel devices, their data is not consistent with D'yakonov Perel spin-orbit relaxation. This discrepancy between our results and theirs is beyond the scope of this work.

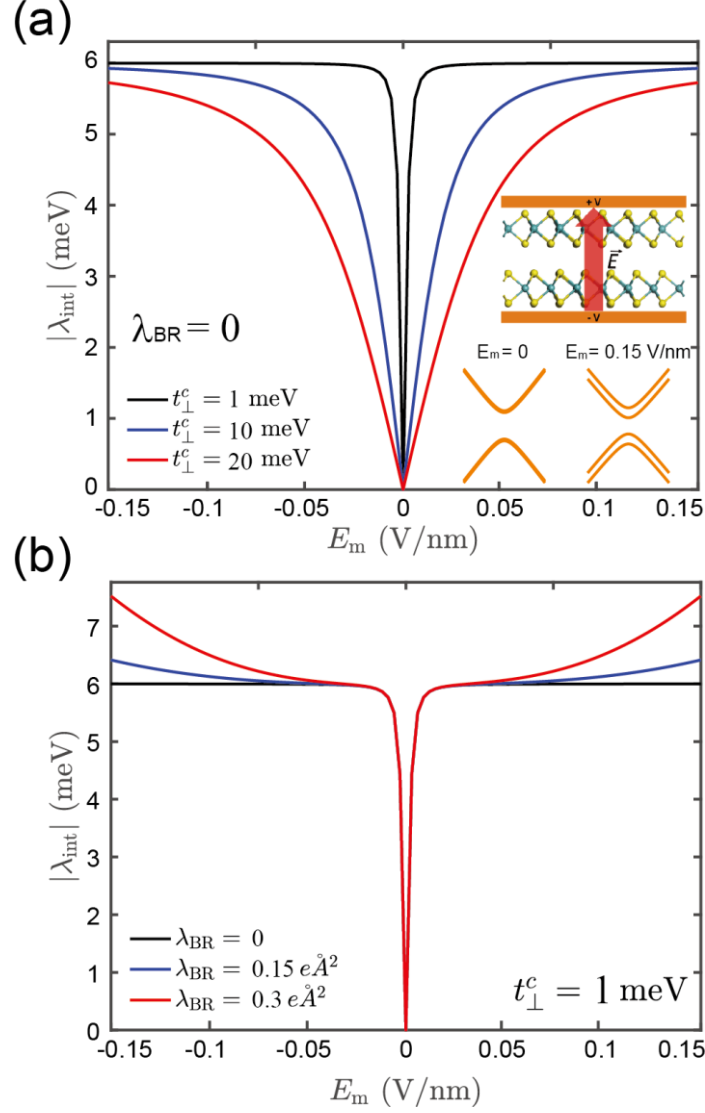


FIG. 1. Theoretical expectation of electric field tunability of spin lifetimes. (a) Theoretical calculation for the effect of conduction band interlayer coupling strength t_{\perp}^c on the tunability of bilayer D'yakonov-Perel spin splitting λ_{int} with an interlayer electric field E_m . At zero electric field, the spin splitting vanishes due to the presence of inversion symmetry and time-reversal symmetry. However, at large electric field, the inversion symmetry is broken, and the spin splitting approaches the single-layer value irrespective of coupling. Insets show a schematic illustration of the vertical

electric field through bilayer MoS₂ (up) and the K-point band structure at $E_m = 0$ and finite E_m (down). (b) Theoretical calculation for the effect of Bychkov-Rashba spin-orbit coupling strength λ_{BR} on the tunability of bilayer λ_{int} with an interlayer coupling strength $t_{\perp}^c = 1$ meV. λ_{int} increases with electric field when λ_{BR} is non-zero, increasing more rapidly with larger λ_{BR} .

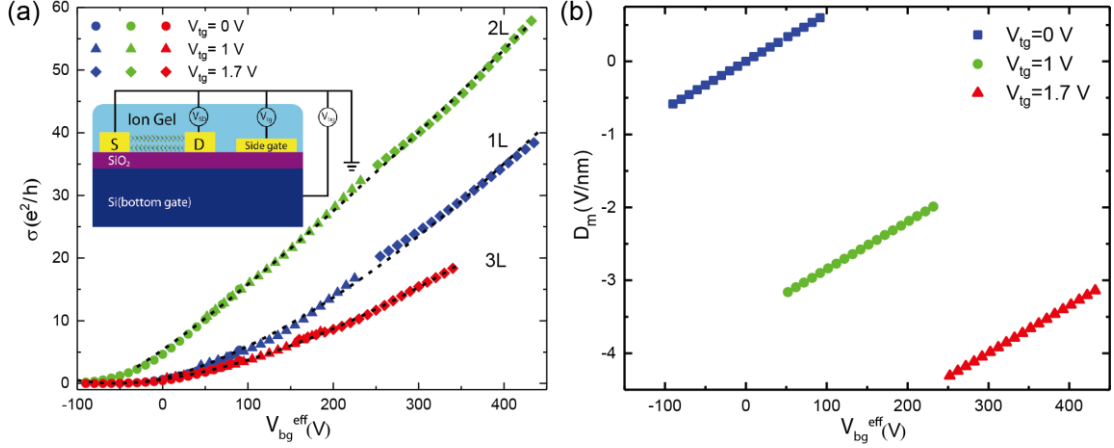


FIG. 2. (a) MoS₂ transfer characteristics for different layer thickness at various combinations of top gate and back-gate voltages. The transfer curves are shifted horizontally according to their conductivity with an indicated effective back-gate voltage bias. Inset shows the schematic illustration of the dual-gated device structure. The dashed lines are fitting curves. (b) Electrical displacement field strength at different combination of the dual gate voltages for simple model which ignores interlayer charge density imbalance.

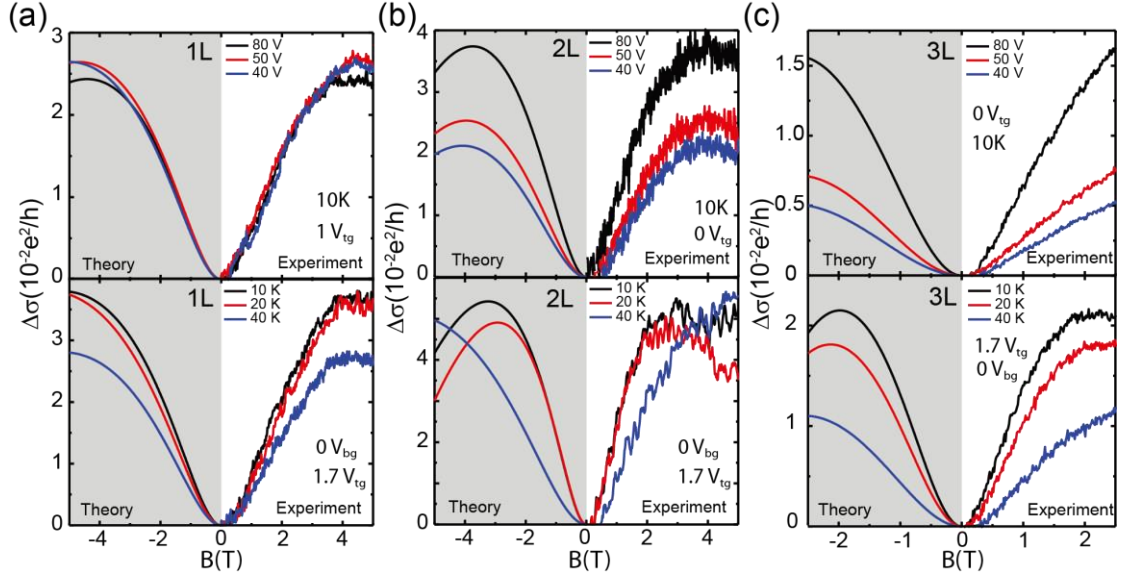


FIG. 3. (a-c) Top panel: Magneto-conductivity of monolayer, bilayer and trilayer MoS₂ at different back-gate voltages of 40, 50, and 80 V and fixed top gate voltage of $V_{tg} = 1$ V(monolayer), $V_{tg} = 0$ V(bilayer and trilayer) and fixed temperature of $T = 10$ K. Bottom panel: Magneto-conductivity of monolayer, bilayer and trilayer MoS₂ at different temperatures of 10, 20, and 40 K and fixed dual gate voltage of $V_{tg} = 1.7$ V, $V_{bg} = 0$ V. The left shaded curves are theoretically fits according to Eq. (1), while right curves in each figure are experimental results. To calculate $\Delta\sigma$, the measured magnetoresistance was symmetrized by $\rho(B) = [\rho(+B) + \rho(-B)]/2$, and that classical quadratic contribution has been subtracted.

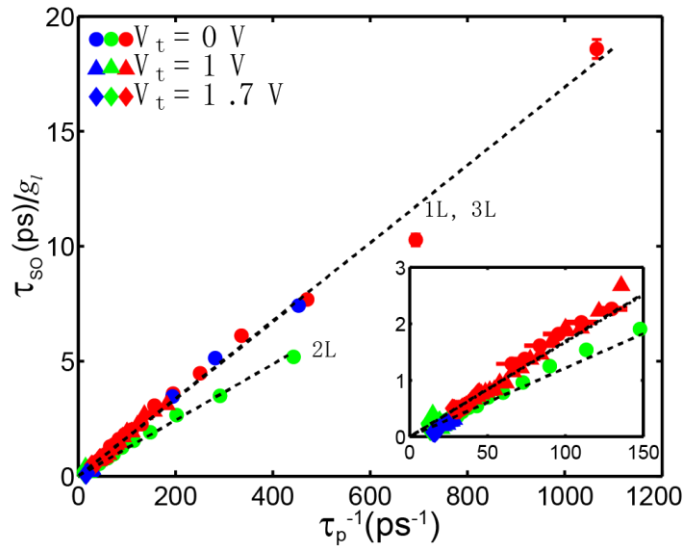


FIG. 4. D'yakonov-Perel spin relaxation in multilayer MoS₂ is electric field independent. The ratios of spin relaxation time τ_{so} with number of layer g_l as a function of inversed momentum relaxation time τ_p^{-1} correspond for monolayer, bilayer, and trilayer MoS₂, respectively. The dashed lines are fits using $2\hbar^2/\tau_p\tau_{so} = \lambda_{\text{int}}^2$. The strength of spin-orbit interaction λ_{int} are found to be 7.2 meV, 6 meV, and 4.1 meV, respectively. Inset shows a zoom in of the low spin relaxation time regime.

ACKNOWLEDGEMENT

We would like to thank Tang Shuai for assistance with the self-consistent screening calculation. G.E. acknowledges support from the Singapore Ministry of Education (MOE) under AcRF Tier 2 (MOE2015-T2-2-123, MOE2017-T2-1-134) and AcRF Tier 1 (R-144-000-387-114). S.A. acknowledges the National University of Singapore Young Investigator Award (R-607-000-094-133). L.C. acknowledges support from National Natural Science Foundation of China (Grant No. 11747169).

References:

- [1] Q. H. Wang, K. Kalantar-Zadeh, A. Kis, J. N. Coleman, and M. S. Strano, *Nature Nanotechnology* **7**, 699 (2012).
- [2] D. Xiao, G. B. Liu, W. Feng, X. Xu, and W. Yao, *Phys Rev Lett* **108**, 196802 (2012).
- [3] X. Xu, W. Yao, D. Xiao, and T. F. Heinz, *Nature Physics* **10**, 343 (2014).
- [4] T. Jungwirth and J. Wunderlich, *Nature Nanotechnology* **9**, 662 (2014).
- [5] K. F. Mak, K. He, J. Shan, and T. F. Heinz, *Nat Nanotechnol* **7**, 494 (2012).
- [6] T. Cao *et al.*, *Nat Commun* **3**, 887 (2012).
- [7] S. Wu *et al.*, *Nature Physics* **9**, 149 (2013).
- [8] A. M. Jones, H. Yu, J. S. Ross, P. Klement, N. J. Ghimire, J. Yan, D. G. Mandrus, W. Yao, and X. Xu, *Nature Physics* **10**, 130 (2014).
- [9] Z. Gong, G.-B. Liu, H. Yu, D. Xiao, X. Cui, X. Xu, and W. Yao, *Nature Communications* **4**, 2053 (2013).
- [10] J. Lee, K. F. Mak, and J. Shan, *Nat Nanotechnol* **11**, 421 (2016).
- [11] Y. J. Zhang, T. Oka, R. Suzuki, J. T. Ye, and Y. Iwasa, *Science* **344**, 725 (2014).
- [12] H. Yuan *et al.*, *Nature Physics* **9**, 563 (2013).
- [13] Y. J. Zhang, W. Shi, J. T. Ye, R. Suzuki, and Y. Iwasa, *Physical Review B* **95**, 205302 (2017).
- [14] D. Costanzo, S. Jo, H. Berger, and A. F. Morpurgo, *Nat Nanotechnol* **11**, 339 (2016).
- [15] X. Cui *et al.*, *Nat Nanotechnol* **10**, 534 (2015).
- [16] A. Kormányos, V. Zólyomi, N. D. Drummond, and G. Burkard, *Physical Review X* **4**, 011034 (2014).
- [17] *See supplementary materials for details.*
- [18] M. M. Fogler and E. McCann, *Physical Review B* **82**, 197401 (2010).
- [19] L. Chu, H. Schmidt, J. Pu, S. Wang, B. Özyilmaz, T. Takenobu, and G. Eda, *Sci Rep* **4**, 7293 (2014).
- [20] H. Schmidt, I. Yudhistira, L. Chu, A. H. Castro Neto, B. Özyilmaz, S. Adam, and G. Eda, *Physical Review Letters* **116**, 046803 (2016).
- [21] M. M. Perera, M.-W. Lin, H.-J. Chuang, B. P. Chamlagain, C. Wang, X. Tan, M. M.-C. Cheng, D. Tománek, and Z. Zhou, *ACS Nano* **7**, 4449 (2013).
- [22] T. Chu, H. Ilatikhameneh, G. Klimeck, R. Rahman, and Z. Chen, *Nano Letters* **15**, 8000 (2015).

- [23] Y. Zhang, T.-T. Tang, C. Girit, Z. Hao, M. C. Martin, A. Zettl, M. F. Crommie, Y. R. Shen, and F. Wang, *Nature* **459**, 820 (2009).
- [24] E. Uesugi, H. Goto, R. Eguchi, A. Fujiwara, and Y. Kubozono, *Sci Rep* **3**, 1595 (2013).
- [25] S. Hikami, A. I. Larkin, and Y. Nagaoka, *Progress of Theoretical Physics* **63**, 707 (1980).
- [26] K. W. Nikos Papadopoulos, Takashi Taniguchi, Herre S. J. van der Zant, and Gary A. Steele, *arXiv:1903.01536*.

Supporting Information for

Phase coherent transport in bilayer and trilayer MoS₂

Leiqiang Chu,^{1,2*} Indra Yudhistira,^{1,3*} Hennrik Schmidt,^{1,3} Tsz Chun Wu,⁵ Shaffique Adam,^{1,3,6,†} and Goki Eda^{1,3,4,‡}

¹*Department of Physics, National University of Singapore, 3 Science Drive 3, Singapore 117543*

²*Department of Physics, Shaoxing University, Shaoxing, China, 312000*

³*Centre for Advanced 2D Materials and Graphene Research Centre, National University of Singapore, 6 Science Drive 2, Singapore 117546*

⁴*Department of Chemistry, National University of Singapore, 2 Science Drive 3, Singapore 117551*

⁵*Department of Physics and Astronomy, Rice University, Houston, Texas 77005, USA*

⁶*Yale-NUS College, 6 College Ave West, Singapore 138614*

1. Theoretical calculation for Figure 1a and 1b.

A minimal model for bilayer MoS₂ can be constructed by adding interlayer hopping to the $\mathbf{k} \cdot \mathbf{p}$ model of monolayers[1],

$$H = \begin{bmatrix} -\frac{U}{2} + \frac{\Delta}{2} + \left(-s_z \frac{\lambda_c}{2} + E_1 \frac{\lambda_{BR}}{2} \mathbf{s} \cdot \mathbf{k}\right) & atke^{i\theta_k} & t_{\perp}^c & 0 \\ atke^{-i\theta_k} & -\frac{U}{2} - \frac{\Delta}{2} + \left(-s_z \frac{\lambda_v}{2} + E_1 \frac{\lambda_{BR}}{2} \mathbf{s} \cdot \mathbf{k}\right) & 0 & t_{\perp}^v \\ t_{\perp}^c & 0 & \frac{U}{2} + \frac{\Delta}{2} + \left(s_z \frac{\lambda_c}{2} + E_2 \frac{\lambda_{BR}}{2} \mathbf{s} \cdot \mathbf{k}\right) & atke^{-i\theta_k} \\ 0 & t_{\perp}^v & atke^{i\theta_k} & \frac{U}{2} - \frac{\Delta}{2} + \left(s_z \frac{\lambda_v}{2} + E_2 \frac{\lambda_{BR}}{2} \mathbf{s} \cdot \mathbf{k}\right) \end{bmatrix} \quad (S1)$$

where Δ is bandgap of monolayer MoS₂, λ_c (λ_v) is the intrinsic spin-orbit coupling (SOC) strength for conduction (valence) band, λ_{BR} is Bychkov-Rashba SOC strength, U is interlayer potential, given by

$$U = eE_m d_m, \quad (S2)$$

with E_m and d_m are interlayer electric field and interlayer distance, respectively, while E_1 (E_2) is the electric field in the bottom (top) layer, given by

$$E_{1(2)} = \frac{E_m + E_{b(t)}}{2}, \quad (S3)$$

where E_b (E_t) are the electric field inside the bottom (top) gate.

We projected the hamiltonian into 2x2 effective Hamiltonian of the conduction band, since in our experiment the sample is electron doped.

$$H_{eff} = \frac{\Delta}{2} + \begin{bmatrix} \frac{\hbar^2 k^2}{2m_1} - \frac{U}{2} - s_z \frac{\lambda_{eff}^{(1)}(k)}{2} & \bar{t}_\perp(k) \\ \bar{t}_\perp(k) & \frac{\hbar^2 k^2}{2m_2} + \frac{U}{2} + s_z \frac{\lambda_{eff}^{(2)}(k)}{2} \end{bmatrix}, (S4)$$

where

$$m_{1(2)} = \frac{\hbar^2}{2a^2 t^2} \frac{\left(\frac{\Delta}{2}\right)^2 - \left(\frac{U}{2}\right)^2 - (t_\perp^v)^2}{\frac{\Delta}{2} \mp \frac{U}{2}}$$

$$\bar{t}_\perp(k) = t_\perp^c + \frac{(atk)^2}{\left(\frac{\Delta}{2}\right)^2 - \left(\frac{U}{2}\right)^2 - (t_\perp^v)^2} t_\perp^v$$

$$\lambda_{eff}^{1(2)} = \sqrt{\lambda_c^2 + (E_{1(2)} \lambda_{BR} k)^2}$$

The energy eigenvalue of the conduction band is then given by

$$E_{\pm, s_z}(k, s_z) = \frac{\Delta}{2} + (atk)^2 \frac{\frac{\Delta}{2}}{\left(\frac{\Delta}{2}\right)^2 - \left(\frac{U}{2}\right)^2 - (t_\perp^v)^2} + s_z \frac{\lambda_{eff}^{(2)}(k) - \lambda_{eff}^{(1)}(k)}{4} \\ \pm \sqrt{\left[\left(1 + \frac{(atk)^2}{\left(\frac{\Delta}{2}\right)^2 - \left(\frac{U}{2}\right)^2 - (t_\perp^v)^2} \right) \frac{U}{2} + s_z \frac{\lambda_{eff}^{(2)}(k) - \lambda_{eff}^{(1)}(k)}{4} \right]^2 + \bar{t}_\perp^2(k)}, (S5)$$

where \pm refers to upper and lower band and s_z for spin up/down.

The spin splitting for the upper and lower band λ_{int}^\pm is then given by

$$\begin{aligned}
\lambda_{int}^{\pm} &= E_{\pm}(s_z = 1) - E_{\pm}(s_z = -1) \\
&= (at)^2(k_{\pm,\uparrow}^2 - k_{\pm,\downarrow}^2) \frac{\frac{\Delta}{2}}{\left(\frac{\Delta}{2}\right)^2 - \left(\frac{U}{2}\right)^2 - (t_{\perp}^v)^2} + \frac{\lambda_{eff}^{(2)}(k_{\pm,\uparrow}) - \lambda_{eff}^{(1)}(k_{\pm,\uparrow})}{4} \\
&\quad + \frac{\lambda_{eff}^{(2)}(k_{\pm,\downarrow}) - \lambda_{eff}^{(1)}(k_{\pm,\downarrow})}{4} \\
&\pm \left\{ \sqrt{\left[\left(1 + \frac{(atk_{\pm,\uparrow})^2}{\left(\frac{\Delta}{2}\right)^2 - \left(\frac{U}{2}\right)^2 - (t_{\perp}^v)^2} \right) \frac{U}{2} + s_z \frac{\lambda_{eff}^{(2)}(k_{\pm,\uparrow}) - \lambda_{eff}^{(1)}(k_{\pm,\uparrow})}{4} \right]^2 + \bar{t}_{\perp}^2(k_{\pm,\uparrow})} \right. \\
&\quad \left. - \sqrt{\left[\left(1 + \frac{(atk_{\pm,\downarrow})^2}{\left(\frac{\Delta}{2}\right)^2 - \left(\frac{U}{2}\right)^2 - (t_{\perp}^v)^2} \right) \frac{U}{2} + s_z \frac{\lambda_{eff}^{(2)}(k_{\pm,\downarrow}) - \lambda_{eff}^{(1)}(k_{\pm,\downarrow})}{4} \right]^2 + \bar{t}_{\perp}^2(k_{\pm,\downarrow})} \right\}, \quad (S6)
\end{aligned}$$

Approximating $k_{\pm,\uparrow} \approx k_{\pm,\downarrow} \equiv k_{\pm}$, we get

$$\begin{aligned}
\lambda_{int}^{\pm} &= \frac{\lambda_{eff}^{(2)}(k_{\pm}) - \lambda_{eff}^{(1)}(k_{\pm})}{2} \\
&\pm \left\{ \sqrt{\left[\left(1 + \frac{(atk_{\pm})^2}{\left(\frac{\Delta}{2}\right)^2 - \left(\frac{U}{2}\right)^2 - (t_{\perp}^v)^2} \right) \frac{U}{2} + \frac{\lambda_{eff}^{(2)}(k_{\pm}, E_m) - \lambda_{eff}^{(1)}(k_{\pm}, E_m)}{4} \right]^2 + \bar{t}_{\perp}^2(k_{\pm}, E_m)} \right. \\
&\quad \left. - \sqrt{\left[\left(1 + \frac{(atk_{\pm})^2}{\left(\frac{\Delta}{2}\right)^2 - \left(\frac{U}{2}\right)^2 - (t_{\perp}^v)^2} \right) \frac{U}{2} - \frac{\lambda_{eff}^{(2)}(k_{\pm}, E_m) - \lambda_{eff}^{(1)}(k_{\pm}, E_m)}{4} \right]^2 + \bar{t}_{\perp}^2(k_{\pm}, E_m)} \right\}, \quad (S7)
\end{aligned}$$

The interlayer electric field E_m is calculated following the screening model of McCann *et al*[2]. We assume that bilayer MoS₂ consists of two parallel conducting plates separated by interlayer distance d_m and dielectric constant κ_m (see Fig. S1). Each layers supports electron densities of n_1 (n_2) for bottom (top) layer, with corresponding back (top) gate held at potential V_b (V_t) with dielectric constant ε_b (ε_t), having thickness of d_b (d_t). Meanwhile, the dielectric constant of bilayer interlayer space is denoted by κ_m .

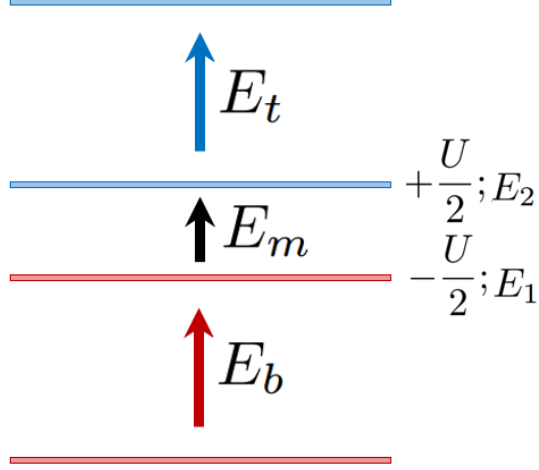


FIG. S1. Schematic of bilayer MoS₂ in the presence of back and top gates.

Application of Gauss' law to the Gaussian surface having cross-sectional area A formed by enclosing both layers, as well as one layer only, yields

$$\varepsilon_0(-\kappa_b E_b + \kappa_t E_t)A = -e(n_1 + n_2)A, (S8a)$$

$$\varepsilon_0(-\kappa_m E_m + \kappa_t E_t)A = -en_2 A, (S8b)$$

respectively, where E_b (E_t) are the electric field inside the bottom (top) gate.

Estimating the electric field of the bottom and top gate as

$$E_{b(t)} \approx \pm \frac{V_{b(t)}}{d_{b(t)}}, (S9)$$

and substitute them to Eq. (S8), we obtain total charge density n and interlayer electric field E_m ,

$$n = n_1 + n_2 = \frac{\varepsilon_0}{e} \left(\frac{\kappa_b V_b}{d_b} + \frac{\kappa_t V_t}{d_t} \right), (S10a)$$

$$E_m = \frac{1}{2d_m} \left(\frac{\alpha_b}{\alpha_m} V_b - \frac{\alpha_t}{\alpha_m} V_t + \frac{\Delta n}{\alpha_m} \right), (S10b)$$

where $\Delta n \equiv n_2 - n_1$ is the charge density imbalance between layers, and α_j is capacitance per area per electron, given by

$$\alpha_j \equiv \frac{C_j}{eA} = \frac{\varepsilon_0 \kappa_j}{e d_j}.$$

Here, subscript j are either t, b , or m for bottom, top, and middle, respectively.

1.1 Non-self-consistent calculation

The simplest estimation of interlayer electric field E_m can be obtained by neglecting interlayer density imbalance (Δn) contribution. This yields

$$\begin{aligned} E_m &\approx \frac{1}{2d_m} \left(\frac{\alpha_b}{\alpha_m} V_b - \frac{\alpha_t}{\alpha_m} V_t \right) \\ &= \frac{1}{2\kappa_m} \left(\kappa_b \frac{V_b}{d_b} - \kappa_t \frac{V_t}{d_t} \right). \end{aligned} \quad (S11)$$

This widely used expression overestimates the interlayer electric field by about an order of magnitude, i.e. ~ 30 times compared to the result of self-consistent calculation [3]. This observation has been considered when we estimate the range of interlayer electric field in Fig. 1a and 1b of the main text.

1.2 Self-consistent calculation

In order to obtain a good quantitative value of interlayer electric field E_m , one need to take the charge density imbalance (Δn) contribution, and solve the equation self-consistently. To obtain the interlayer charge density imbalance Δn , the charge density in each layer $n_{1(2)}$ is calculated by integration over Fermi surface taking into account the probability of occupancy in each layer

$$\begin{aligned} n_1^{c\pm} &= 4 \int_0^{k_F^\pm} \frac{d^2 k}{(2\pi)^2} \left(|\psi_1^{c,\pm}(k, E_m)|^2 + |\psi_2^{c,\pm}(k, E_m)|^2 \right), \quad (S12) \\ n_2^{c\pm} &= 4 \int_0^{k_F^\pm} \frac{d^2 k}{(2\pi)^2} \left(|\psi_3^{c,\pm}(k, E_m)|^2 + |\psi_4^{c,\pm}(k, E_m)|^2 \right) \\ n_1^{v\pm} &= 4 \int_0^{k_{max}} \frac{d^2 k}{(2\pi)^2} \left(|\psi_1^{v,\pm}(k, E_m)|^2 + |\psi_2^{v,\pm}(k, E_m)|^2 \right) \\ &\quad - 4 \int_0^{k_{max}} \frac{d^2 k}{(2\pi)^2} \left(|\psi_1^{v,\pm}(k, E_m = 0)|^2 + |\psi_2^{v,\pm}(k, E_m = 0)|^2 \right) \end{aligned}$$

$$n_2^{v\pm} = 4 \int_0^{k_{max}} \frac{d^2k}{(2\pi)^2} \left(|\psi_3^{v,\pm}(k, E_m)|^2 + |\psi_4^{v,\pm}(k, E_m)|^2 \right) \\ - 4 \int_0^{k_{max}} \frac{d^2k}{(2\pi)^2} \left(|\psi_3^{v,\pm}(k, E_m = 0)|^2 + |\psi_4^{v,\pm}(k, E_m = 0)|^2 \right),$$

where the superscript $c(v)$ refers to conduction (valence) band, the \pm sign refers to the higher (lower) band, $\psi_j^{c(v),\pm}$ with $j=1,2,3,4$ are components of eigenvector $\Psi^{c(v),\pm} = \left(\psi_1^{c(v),\pm} \psi_2^{c(v),\pm} \psi_3^{c(v),\pm} \psi_4^{c(v),\pm} \right)^T$, and $k_{max} \sim O(2\pi/a)$ is ultraviolet cutoff. Here a is size of unit cell.

For this interlayer electric field (E_m) calculation, we have used the original 4x4 effective Hamiltonian of Eq. (S1) with $\lambda_c \approx \lambda_{BR} \approx 0$ approximation.

Combining contribution from both conduction and valence band, we obtain individual layer density

$$n_{1(2)} = \begin{cases} n_{1(2)}^{c-} + n_{1(2)}^{v-} + n_{1(2)}^{v+} & ; \text{if } E_F < \Delta/2 + \sqrt{t_c^2 + (U/2)^2} \\ n_{1(2)}^{c-} + n_{1(2)}^{c+} + n_{1(2)}^{v-} + n_{1(2)}^{v+} & ; \text{otherwise} \end{cases}, \quad (S13)$$

Here, we have assumed that E_F lies in conduction band, in accordance with the condition in our experiment.

Interlayer electric field E_m is obtained by solving self-consistently Eq. (S10b), with Δn calculated using Eq. (S12) and Eq. (S13).

Finally, one needs these equations to close the self-consistency equation.

$$\begin{cases} k_F^- = \sqrt{\pi n} & ; \text{if } E_F < \Delta/2 + \sqrt{t_c^2 + (U/2)^2} \\ (k_F^-)^2 + (k_F^+)^2 = \pi n & \\ E_-(k_F^-, E_m) = E_+(k_F^+, E_m) & ; \text{otherwise} \end{cases}, \quad (S14)$$

2. Determination of V_0 .

To determine V_0 , we first extract the phase coherence length L_ϕ by fitting the quantum transport data with HLN theory. We then plot it as a function of the effective back-gate voltage V_{bg}^{eff} , as shown in Figure S2. Finally, V_0 is obtained from linear extrapolation to $L_\phi = 0$.

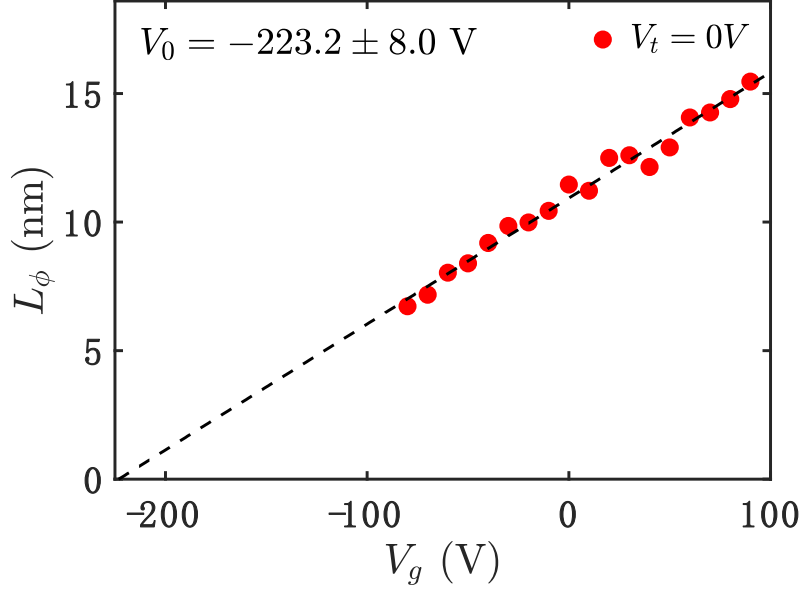


FIG. S2. Phase coherence length of bilayer MoS₂ as a function of effective back gate voltage.

3. Procedure for extract the pure quantum interference effect.

The magnetoresistance(MR) is defined as:

$$MR(B) = \frac{R(B) - R(0)}{R(0)} \times 100\%, (S15)$$

where $R(B)$ is the sheet resistance at a given magnetic field B .

Ordinary magnetoresistance (OMR) is a classical effect due to cyclic motion of the electrons. It typically follows kohler's rule:

$$MR \sim (\omega_c \tau)^2 = (\mu B)^2, (S16)$$

where ω_c is the cyclotron frequency, τ is the momentum scattering time, and μ is the carrier mobility. As shown in Figure S3, a quadratic fitting collapse well with the MR at high magnetic field, indicating our MR at high field contains contributions from both classical and quantum interference effects. We subtract the classical background to reveal the pure quantum correction as shown in the inset red curve. To further verify our assumption of the OMR at high field, we plot MR as a function with B^2 . As

shown in Fig. S1b, the data collapse well on a single linear curve for $B > 4$ T for various gate-voltage combinations. The curves are normalized according to the quadratic fitting to show their consistent linear behaviour at high magnetic field.

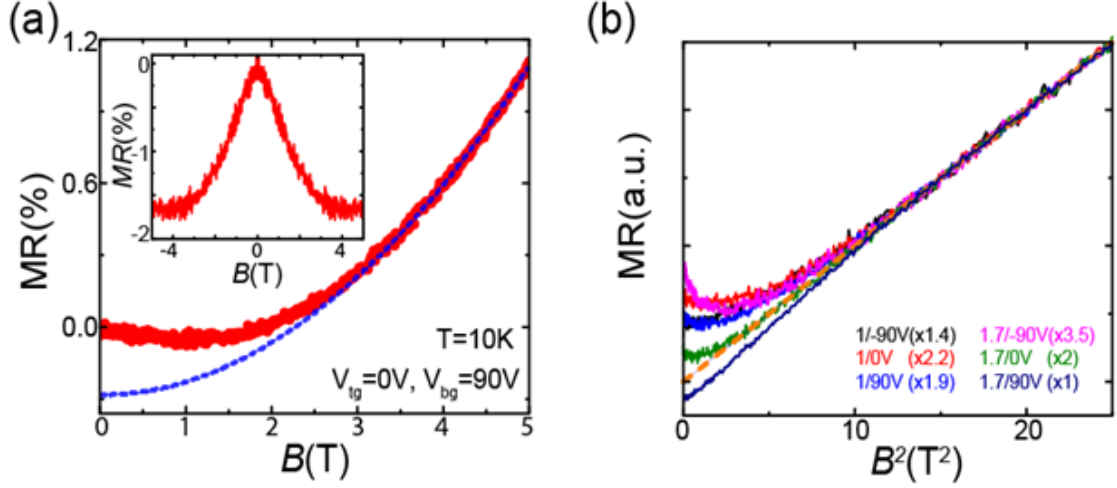


FIG. S3. Classical and quantum corrections. (a) Magnetoresistance at high field contains a quadratic classical contribution, as indicated by the fitting dashed blue line. The inset shows the calculated contribution from pure quantum interference effect after subtraction of the classical background. In the main text, the magneto-transport data shown are all pure quantum contributions. (b) MR scales as a function of B^2 for several combinations of dual gate voltages. The curves are all normalized by multiplying factors (shown in the brackets). As indicated by the orange dashed line, it is apparently linear for all curves at high magnetic fields.

References

1. Gong, Z., et al., *Magnetoelectric effects and valley-controlled spin quantum gates in transition metal dichalcogenide bilayers*. Nature Communications, 2013. **4**: p. 2053.
2. Fogler, M.M. and E. McCann, *Comment on "Screening in gated bilayer graphene"*. Physical Review B, 2010. **82**(19): p. 197401.
3. Shuai, T. *Theoretical and experimental investigations of some factors influencing the energy levels of bilayer and multilayer MoS_2* . <http://scholarbank.nus.edu.sg/handle/10635/151253>